24

Probing Ultrafast Dynamics of Polarization Clusters in $BaTiO_3$ by Pulsed Soft X-Ray Laser Speckle Technique

Kai Ji[1] and Keiichiro Nasu[2]
[1]*Institute for Theoretical Physics and Heidelberg Center for Quantum Dynamics*
University of Heidelberg
Philosophenweg 19, 69120 Heidelberg
Germany
[2]*Photon Factory, Institute of Materials Structure Science*
High Energy Accelerator Research Organization
Graduate University for Advanced Studies
Oho 1-1, Tsukuba, Ibaraki 305-0801
Japan

1. Introduction

The technical development of ultrashort laser pulses covering infrared to extreme ultraviolet has opened a door to study the photo-induced dynamic physical and chemical processes. By using an optical excitation at a particular wavelength, exotic states can be trigged coherently in atoms, molecules, clusters as well as complex condensed systems. The evolution of excited states then can be imaged in the real-time domain by subsequent single or trains of pulse. This laser pump-probe technique features an unprecedented spatial and temporal resolution, thus not only allows us a fundamental insight into the microscopic ultrafast dynamics, but also brings about a potential of selective controlling on the microstructures at atomic scale (Krausz & Ivanov, 2009).

In this chapter, a recent advance of soft x-ray laser speckle pump-probe measurement on barium titanate ($BaTiO_3$) is reviewed, with primary concerns on the theoretical description of the photo-matter interaction and photo-induced relaxation dynamics in the crystal. Here, the observed time-dependent speckle pattern is theoretically investigated as a correlated optical response to the pump and probe pulses. The scattering probability is calculated based on a model with coupled soft x-ray photon and ferroelectric phonon mode of $BaTiO_3$. It is found that the speckle variation is related with the relaxation dynamics of ferroelectric clusters created by the pump pulse. Additionally, a critical slowing down of cluster relaxation arises on decreasing temperature towards the paraelectric-ferroelectric transition temperature. Relation between the critical slowing down, local dipole fluctuation and crystal structure are revealed by a quantum Monte Carlo simulation.

This chapter is organized as follows. In Section 1, the properties ferroelectric material and experimental techniques are introduced. The theoretical model and methods are elaborated in Section 2. In Section 3, the numerical results on speckle correlation, relaxation dynamics

Source: Coherence and Ultrashort Pulse Laser Emission, Book edited by: Dr. F. J. Duarte,
ISBN 978-953-307-242-5, pp. 688, December 2010, InTech, Croatia, downloaded from InTech.com

of polarization cluster and critical slowing down are discussed in details. In Section 4, a summary with conclusion is presented finally.

1.1 General properties of $BaTiO_3$

As a prototype of the ferroelectric perovskite compounds, $BaTiO_3$ undergoes a transition from paraelectric cubic to ferroelectric tetragonal phase at Curie temperature T_c=395 K. As schematically shown in Fig. 1, above T_c, the geometric centers of the Ti^{4+}, Ba^{2+} and O^{2-} ions coincide, giving rise to a non-polar lattice. Below T_c, the unit cell is elongated along the c axis with a ratio c/a~1.01. The Ti^{4+} and Ba^{2+} ions are displaced from their geometric centers with respect to the O^{2-} ions, to give a net polarity to the lattice. The formation of spontaneous polarization by the displacement of ions is along one of the [001] directions in the original cubic structure. Thus, below T_c, there are two kinds of ferroelectric domain developed with mutually perpendicular polarization (Yin et al., 1006). The paraelectric-ferroelectric phase transition and domain induced static surface corrugation have been well resolved by the means of atomic force microscopy (Hamazaki et al., 1995), scanning probe microscopy (Pang et al., 1998), neutron scattering (Yamada et al., 1969), and polarizing optical microscopy (Mulvmill et al., 1996).

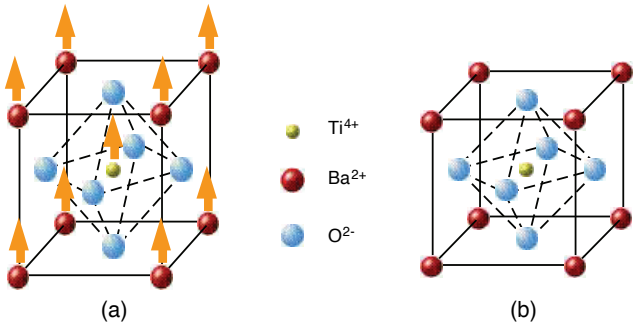

Fig. 1. The crystal structure of $BaTiO_3$ (a) below the Curie temperature the structure is tetragonal with Ba^{2+} and Ti^{4+} ions displaced relative to O^{2-} ions; (b) above the Curie temperature the cell is cubic.

Ferroelectric materials have a variety of functional capabilities in the electronic devices, which include non-volatile memory, high permittivity capacitor, actuator and insulator for field-effect transistor (Polla et al., 1998). Application of ferroelectric materials has attracted a great deal of attention in recent years to enhance the performance of implementation. This requires a comprehensive knowledge concerning the behaviours of ferroelectrics at the nanoscale, such as the roles of strain, deploarization fields, domain configurations and motions. Besides, there is also an increased demand to understand the mechanism of paraelectric-ferroelectric phase transition. In the case of $BaTiO_3$, it is generally considered that the transition is a classic displacive soft-mode type, which is driven by the anharmonic lattice dynamics (Harada et al., 1971; Migoni et al., 1976). However, recent studies have also suggested that there might be an order-disorder instability which coexists with the displacive transition (Zalar et al., 2003; Völkel & Müller, 2007), making this issue still controversial to date.

The nature of the phase transition is believed to be unveiled in the precursor phenomena. For $BaTiO_3$, this is the emergence of dipole fluctuations with regional uniform alignments,

i.e. the polarization clusters (Takagi & Ishidate, 2000). While, it is still not clear how these polarization fluctuations condense into long range ferroelectric correlations as temperature decreases. Therefore, it is of great significance to directly observe the creation and evolution of polarization cluster in the vicinity of T_c.

1.2 Experimental methodology

Since the aforementioned conventional time-average-based measurements cannot be applied to detect the ultrafast transient status of dipole clusters, the diffraction speckle pattern of $BaTiO_3$ crystal captured by the picosecond soft x-ray laser has turned out to be an efficient way.

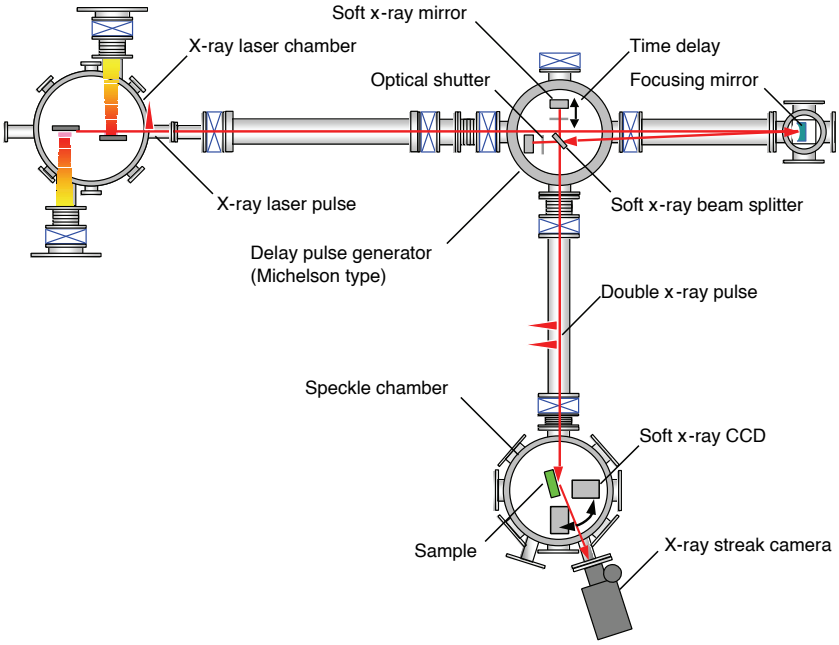

Fig. 2. Schematic diagram of soft x-ray speckle pump-probe spectroscopy system using a Michelson type delay pulse generator and a soft x-ray streak camera. All the optical components are set in a vacuum (~10^{-4} Pa). The delay time of the second x-ray pulse from the first one can be manipulated by changing the delay path length between the beam splitter and x-ray mirror.

Speckle is the random granular pattern produced when a coherent light is scattered off a rough surface. It carries information of the specimen surface, for the intensity and contrast of the speckle image vary with the roughness of surface being illuminated (May, 1977). Numerous approaches have been devised to identify surface profiles by either the speckle contrast or the speckle correlation method (Goodman, 2007). Recent application of pulsed soft x-ray laser has improved the temporal and spatial resolution to a scale of picosecond and nanometer. By this means, dynamics of surface polarization clusters of $BaTiO_3$ across the Curie temperature has been observed (Tai et al., 2002; Tai et al., 2004), which paves a new way to study the paraelectric-ferroelectric phase transition.

Very recently, Namikawa (Namikawa et al., 2009) study the polarization clusters in $BaTiO_3$ at above T_c by the plasma-based x-ray laser speckle measurement in combination with the technique of pump probe spectroscopy. In this experiment, as shown in Fig. 2, two consecutive soft x-ray laser pulses with wavelength of 160 Å and an adjustable time difference are generated coherently by a Michelson type beam splitter (Kishimoto et al., 2010). After the photo excitation by the pump pulse, ferroelectric clusters of nano scale are created in the paraelectric $BaTiO_3$ and tends to be smeared out gradually on the way back to the equilibrium paraelectric state. This relaxation of cluster thus can be reflected in the variation of speckle intensity of the probe pulse as a function of its delay time from the first pulse. It has been observed that the intensity of speckle pattern decays as the delay time increases. Moreover, the decay rate also decreases upon approaching T_c, indicating a critical slowing down of the cluster relaxation time. Hence, by measuring the correlation between two soft x-ray laser pulses, the real time relaxation dynamics of polarization clusters in $BaTiO_3$ is clearly represented. In comparison with other time-resolved spectroscopic study on $BaTiO_3$, for example the photon correlation spectroscopy with visible laser beam (Yan et al., 2008), Namikawa's experiment employs pulsed soft x-ray laser as the light source. For this sake, the size of photo-created ferroelectric cluster is reduced to a few nanometers, and the cluster relaxation time is at a scale of picosecond. This measurement, thus, uncovers new critical properties of the ultrafast relaxation dynamics of polarization clusters.

2. Theoretical model and methods

In this and next sections, we examine the newly reported novel behaviours of ferroelectric cluster observed by Namikawa from a theoretical point of view, aiming to provide a basis for understanding the critical nature of $BaTiO_3$. Theoretically, the dynamics of a system can be adequately described by the linear response theory, i.e., to express the dynamic quantities in terms of time correlation functions of the corresponding dynamic operators. In general, the path integral quantum Monte Carlo method is computationally feasible to handle the quantum many body problems, for it allows the system to be treated without making any approximation. However, simulation on real time dynamics with Monte Carlo method is still an open problem in computational physics because of the formidable numerical cost of path summation which grows exponentially with the propagation time. The common approach to circumvent this problem is to perform imaginary time path integration followed by analytic continuation, and to compute the real time dynamic quantities using Fourier transformation. In the present study, the real time correlation functions and real time dependence of speckle pattern are investigated following this scheme (Ji et al., 2009).

2.1 Model Hamiltonian

Theoretical interpretations for structural phase transition and domain wall dynamics have be well established in the framework of Krumhansl-Schrieffer model (also known as φ^4 model) (Krumhansl & Schrieffer, 1975; Aubry, 1975; Schneider & Stoll, 1978; Savkin et al., 2002). In this model, the particles are subject to anharmonic on-site potentials and harmonic inter-site couplings. The on-site potential is represented as a polynomial form of the order parameter such as polarization, displacement, or elasticity, which displays a substantial change around T_c. Since the φ^4 model is only limited to second-order transitions, in the present work we invoke a modified Krumhansl-Schrieffer model (also called φ^6 model) (Morris & Gooding, 1990; Khare & Saxena, 2008) to study the first-order ferroelectric phase

transition of $BaTiO_3$. In this scenario, the Hamiltonian of $BaTiO_3$ crystal ($\equiv H_f$) is written as (here we let $\hbar$=1),

$$H_f = -\frac{\omega_0}{2}\sum_l \frac{\partial^2}{\partial^2 Q_l^2} + U_0 + U_i \,, \tag{1}$$

$$U_0 = \frac{\omega_0}{2}\sum_l \left(Q_l^2 - c_4 Q_l^4 + \frac{c_6}{3} Q_l^6 \right), \tag{2}$$

$$U_i = -\frac{\omega_0 d_2}{2} \sum_{<l,l'>} Q_l Q_{l'} \,, \tag{3}$$

where, U_0 and U_i are the on-site potential and inter-site correlation, respectively. Q_l is the coordinate operator for the electric dipole moment due to a shift of titanium ions against oxygen ions, i.e., the T_{1u} transverse optical phonon mode. ω_0 is the dipole oscillatory frequency, l labels the site, and <l,l'> in Eq. (3) enumerates the nearest neighboring pairs.
In order to describe the optical response of $BaTiO_3$ due to x-ray scattering, we design a theoretical model to incorporate the radiation field and a weak interplay between radiation and crystal. The total Hamiltonian reads,

$$H = H_p + H_f + H_{pf} \,, \tag{4}$$

$$H_p = \sum_k \Omega_k a_k^+ a_k \,,\ \Omega_k = c|k| \,. \tag{5}$$

Eq. (5) represents the polarized light field, where a_k^+ (a_k) is the creation (annihilation) operator of a photon with a wave number k and an energy Ω_k, and c is the light velocity in vacuum. In Namikawa's experiment, the wave length of x-ray is 160 Å, thus the photon energy is about 80 eV. Denoting the odd parity of T_{1u} mode, the photon-phonon scattering is of a bi-linear Raman type,

$$H_{pf} = \frac{V}{N} \sum_{q,q',k} a^+_{k+\frac{q}{2}} a_{k-\frac{q}{2}} Q_{q'-\frac{q}{2}} Q_{-q'-\frac{q}{2}} \,, \tag{6}$$

where V is the photon-phonon coupling strength, Q_q ($\equiv N^{-1/2}\Sigma_l e^{-iql} Q_l$) the Fourier component of Q_l with a wave number q. Without losing generalitivity, here we use a simple cubic lattice, and the total number of lattice site is N.

2.2 Optical response to pump and probe photons

Since there are two photons involved in the scattering, the photon-phonon scattering probability can be written as,

$$P(t) = \sum_{k_1,k_1'} \left\langle\!\left\langle a_{k_0}(0) a_{k_1}^+(\Delta) a_{k_0}(t) a_{k_1'}^+(\Delta+t) a_{k_1'}(\Delta+t) a_{k_0}^+(t) a_{k_1}(\Delta) a_{k_0}^+(0) \right\rangle\!\right\rangle \,, \tag{7}$$

where

$$\left\langle\!\left\langle \cdots \right\rangle\!\right\rangle = \mathrm{Tr}\left(e^{-\beta H} \cdots\right) / \mathrm{Tr}\left(e^{-\beta H}\right) \tag{8}$$

means the expectation, $\beta(\equiv 1/k_B T)$ is the inverse temperature, and the time dependent operators are defined in the Heisenberg representation,

$$O(t) = e^{itH} O e^{-itH} , \tag{9}$$

Here, t denotes the time difference between two incident laser pulses as manifested in Fig. 3, and k_0 the wave number of incoming photon. After a small time interval Δ, the photon is scattered out of the crystal. k_1 and k_0' are the wave numbers of the first and second outgoing photons, respectively.

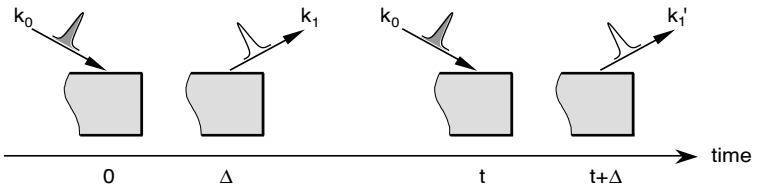

Fig. 3. Pulse sequence in an x-ray laser speckle experiment. The pump and probe pulses of k_0 creates and detects ferroelectric clusters in the sample of paraelectric $BaTiO_3$, respectively, and generate new x-ray fields in the direction k_1 and k_0' after a short time interval Δ.

Treating H_{pf} as a perturbation, we separate Hamiltonian of Eq. (4) as,

$$H = H_0 + H_{pf} , \tag{10}$$

where

$$H_0 = H_p + H_f , \tag{11}$$

is treated as the unperturbed Hamiltonian. By expanding the time evolution operator in Eq. (9) with respect to H_{pf} ,

$$e^{-itH} \to e^{-itH_0}\left[1 - i\int_0^t dt_1 \hat{H}_{pf}(t_1) + \cdots\right], \tag{12}$$

we find that the lowest order terms which directly depend on t are of fourth order,

$$P(t) \to \int_0^\Delta dt_1 \int_0^\Delta dt_2 \int_0^\Delta dt_1' \int_0^\Delta dt_2' \sum_{k_1, k_1'} \left\langle\left\langle a_{k_0} \hat{H}_{pf}(t_1') e^{i\Delta H_0} a_{k_1}^+ e^{i(t-\Delta)H_f} a_{k_0} \hat{H}_{pf}(t_2') e^{i\Delta H_0} a_{k_1'}^+ \right.\right.$$

$$\left.\left. \times a_{k_1'} e^{-i\Delta H_0} \hat{H}_{pf}(t_2) a_{k_0}^+ e^{-i(t-\Delta)H_f} a_{k_1} e^{-i\Delta H_0} \hat{H}_{pf}(t_1) a_{k_0}^+ \right\rangle\right\rangle , \tag{13}$$

where the operators with carets are defined in the interaction representation,

$$\hat{O}(t) = e^{itH_0} O e^{-itH_0} . \tag{14}$$

Fig. 4 represents a diagram analysis for this phonon-coupled scattering process, where photons (phonons) are depicted by the wavy (dashed) lines, and the upper (lower)

horizontal time lines are corresponding to the bra (ket) vectors (Nasu, 1994). Diagram (a) illustrates the changes of wave number and energy of photons due to the emitted or absorbed phonons. This is noting but the Stokes and anti-Stokes Raman scattering. Whereas, diagrams (b)-(f) are corresponding to the exchange, side band, rapid damping, rapid exchange and mutual damping effects, respectively.

Obviously, diagram (c) brings no time dependence, while diagrams (d), (e) and (f) only contributes a rapid reduction to the time correlation of two laser pulses because of the duality in phonon interchange. In this sense, the time dependence is primarily determined by the diagrams (a) and (b). Thus, the scattering probability turns out to be,

$$P(t)=\int_0^{\Delta}dt_1\int_0^{\Delta}dt_2\int_0^{\Delta}dt_1'\int_0^{\Delta}dt_2'\,\frac{2V^4}{N^4}\sum_{q,q'}\Big\langle\Big\langle a_{k_0}e^{it_1'H_p}a_{k_0}^{+}a_{k_0-q}e^{-i(t_1'-\Delta)H_p}a_{k_0-q}^{+}$$

$$\times a_{k_0}e^{it_2'H_p}a_{k_0}^{+}a_{k_0+q}e^{-i(t_2'-\Delta)H_p}a_{k_0+q}^{+}a_{k_0+q}e^{i(t_2-\Delta)H_p}a_{k_0+q}^{+}a_{k_0}e^{-it_2H_p}a_{k_0}^{+}$$

$$\times a_{k_0-q}e^{i(t_1-\Delta)H_p}a_{k_0-q}^{+}a_{k_0}e^{-it_1H_p}a_{k_0}^{+}\Big\rangle\Big\rangle\Big\langle\Big\langle\hat{Q}_{q'}(t_1')\hat{Q}_{q-q'}(t_1')\hat{Q}_{-q+q'}(t+t_2')$$

$$\times\hat{Q}_{-q'}(t+t_2')\hat{Q}_{q'}(t+t_2')\hat{Q}_{q-q'}(t+t_2)\hat{Q}_{-q+q'}(t_1)\hat{Q}_{-q'}(t_1)\Big\rangle\Big\rangle, \tag{15}$$

where the photons and phonons are decoupled, and it becomes evident that the origin of the *t*-dependence is nothing but the phonon (dipole) correlation.

Since the photonic part in Eq. (15) is actually time-independent, and in the case of forward x-ray scattering we have $|k_0|\approx|k_1|\approx|k_1'|$, the normalized probability can be simplified as,

$$\frac{P(t)}{P(0)}=\frac{\sum_{q,q'}\Big|\Big\langle\Big\langle Q_q^2\Big\rangle\Big\rangle G_{q+q'}(t)\Big|^2}{\sum_{q,q'}\Big|\Big\langle\Big\langle Q_q^2Q_{q+q'}^2\Big\rangle\Big\rangle\Big|^2}, \tag{16}$$

where

$$G_q(t)=-i2\Big\langle\Big\langle T\hat{Q}_q(t)\hat{Q}_{-q}(0)\Big\rangle\Big\rangle, \tag{17}$$

is the real time Green's function of phonon, and T the time ordering operator. In deriving Eq. (16), we have also made use of the fact that the light propagation time in the crystal is rather short. The Fourier component of Green's function,

$$G_q(\omega)=\int_{-\infty}^{\infty}dt\;G_q(t)\;e^{-i\omega t}, \tag{18}$$

is related to the phonon spectral function [$\equiv A_q(\omega)$] through (Doniach & Sondheimer, 1998),

$$G_q(\omega)=\int_{-\infty}^{\infty}\frac{d\omega'}{2\pi}\frac{A_q(\omega')}{1-\exp(-\beta\omega')}\left[\frac{1}{\omega-\omega'+i0^+}-\frac{\exp(-\beta\omega')}{\omega-\omega'-i0^+}\right], \tag{19}$$

The phonon spectral function describes the response of lattice to the external perturbation, yielding profound information about dynamic properties of the crystal under investigation.

Once we get the spectral function, the scattering probability and correlation function can be readily derived.

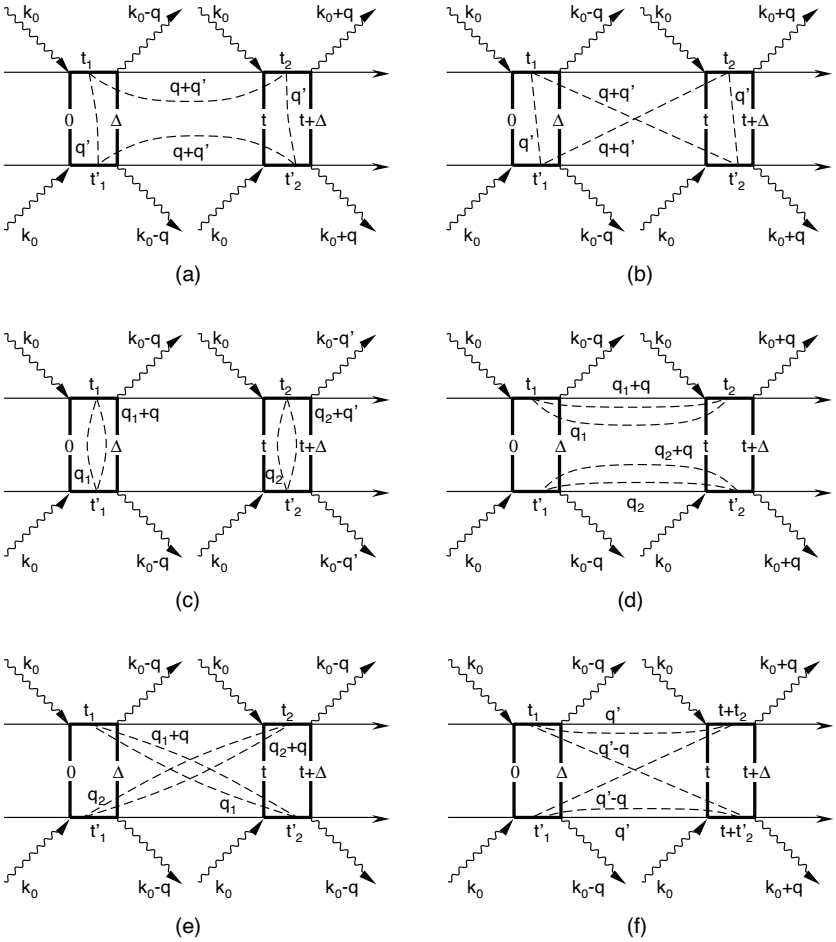

Fig. 4. Double-sided Feynman diagrams for scattering process of photon with electric dipole moment (phonon). The photons and phonons are denoted by the wavy and dashed lines, respectively. In each diagram, the upper and lower horizontal time lines represent the bra and ket vectors, respectively.

2.3 Dynamics of crystal

A mathematically tractable approach to spectral function $A_q(\omega)$ is to introduce an imaginary time phonon Green's function, for it can be evaluated more easily than its real time counterpart. In the real space, the imaginary time Green's function is defined as,

$$G_{ll'}(\tau) \equiv -2\left\langle\left\langle T\hat{Q}_l(\tau)\hat{Q}_{l'}(0)\right\rangle\right\rangle, \tag{20}$$

where $\tau(\equiv it)$ is the argument for imaginary time (unless otherwise noted, we use Roman t for real time and Greek τ for imaginary time). The imaginary time dependence of an operator in the interaction representation is given by

$$\hat{O}(\tau) = e^{i\tau H_0} O e^{-i\tau H_0} . \tag{21}$$

Under the weak coupling approximation, and by using the Suzuki-Trotter identity, the Green's function can be rewritten into a path integral form (here we assume τ>0) (Ji et al., 2004),

$$G_{ll''}(\tau) = \int Dx \; e^{-\beta[\Phi_f(x)-\Phi_f]}\left[-2x_l(\tau)x_{l''}(0)\right]. \tag{22}$$

where x_l is the eigenvalue of Q_l,

$$Q_l \left| x_l \right\rangle = x_l \left| x_l \right\rangle , \tag{23}$$

$\Phi_f(x)$ is the path-dependent phonon free energy,

$$e^{-\beta\,\Phi_f(x)} = e^{-\int_0^\beta d\tau\; \Omega_f[x(\tau)]} , \tag{24}$$

with

$$\Omega_f = -\sum_l \left[\frac{1}{2\omega_0}\left(\frac{\partial x_l}{\partial \tau}\right)^2 + \frac{1}{2}\omega_0 x_l^2 - \frac{1}{2}\omega_0 c_4 x_l^4 + \frac{1}{6}\omega_0 c_6 x_l^6 \right] - \frac{1}{2}\omega_0 d_2 \sum_{<l,l'>} x_l x_l' , \tag{25}$$

and Ω_f is the total phonon free energy,

$$e^{-\beta\,\Phi_f} = \int Dx \; e^{-\beta\,\Phi_f(x)} . \tag{26}$$

In the path integral notation, the internal energy of crystal E_f ($\equiv \left\langle\left\langle H_f \right\rangle\right\rangle$ is represented as

$$\Omega_f = \int Dx \; e^{-\beta\,[\Phi_f(x)-\Phi_f]} \left[\omega_0 \sum_l \left(x_l^2 - \frac{3}{2}c_4 x_l^4 + \frac{2}{3}c_6 x_l^6 \right) - \omega_0 d_2 \sum_{<l,l'>} x_l x_l' \right], \tag{27}$$

from which the heat capacity can be derived as

$$C_f^V = \left(\frac{\partial E_f}{\partial T} \right)_V . \tag{28}$$

The Green's function of momentum space is given by,

$$G_q(\tau) = \frac{1}{N}\sum_{l,l''} e^{iq(l-l'')}\; G_{ll''}(\tau) , \tag{29}$$

which is connected with the phonon spectral function $A_q(\omega)$ through (Bonča & Gubernatis, 1996)

$$G_q(\tau) = -\int_0^\infty \frac{\cosh\left[\left(\frac{1}{2}\beta - \tau\right)\omega\right]}{\sinh\left(\frac{1}{2}\beta\omega\right)} A_q(\omega) d\omega \,. \tag{30}$$

Solving this integral equation is a notoriously ill-posed numerical problem because of the highly singular nature of the kernel. In order to analytically continue the imaginary time data into real frequency information, specialized methods are developed, such as maximum entropy method (Skilling, 1984) and least squares fitting method (Yamazaki et al., 2003). Ji (Ji et al., 2004) develops an iterative fitting approach to derive the electron spectral function, which gives a rapid and stable convergence of the spectrum without using any prior knowledge or artificial parameter. In the present study, however, the phonon spectral function does not yield a specific sum rule like the case of electron, the iterative fitting method cannot be applied directly. For this sake, we have modified this method by a renormalized iteration algorithm (Ji et al., 2009). Details of the standard and renormalized iterative fitting methods can be found in Appendices 6.2 and 6.3, respectively.

3. Numerical results and discussion

3.1 Optical responses

Based on the path integral formalisms, the imaginary time Green's function can be readily calculated via a standard quantum Monte Carlo simulation (Ji et al., 2004). Our numerical calculation is performed on a 10×10×10 cubic lattice with a periodic boundary condition. The imaginary time is discretized into 10-20 infinitesimal slices. As already noticed for the analytic continuation (Gubernatis et al., 1991), if the imaginary time Green's function is noisy, the uncertainty involved in the inverse transform might be very large, and the spectral function cannot be determined uniquely. In order to obtain accurate data from quantum Monte Carlo simulation, a hybrid algorithm (Ji et al., 2004) has been implemented in our calculation. This method is elaborated in the Appendix 6.1. Besides, we pick out each Monte Carlo sample after 100-200 steps to reduce the correlation between adjacent configurations. The Monte Carlo data are divided into 5-10 sets, from which the 95% confidence interval is estimated through 10,000 resampled set averages by the percentile bootstrap method. We found that about 1,000,000 Monte Carlo configurations are sufficient to get well converged spectral functions and real time dynamic quantities.

In the numerical calculation, the phonon frequency ω_0 is assumed to be 20 meV (Zhong et al., 1994), the inter-site coupling constant d_2 is fixed at a value of 0.032, whereas c_4 and c_6 are selected to make the on-site U_0 a symmetric triple-well potential. As shown in Fig. 5, this triple-well structure is featured by five potential extrema located at x_a, $\pm x_b$ and $\pm x_c$, where

$$x_a = 0 \,, \tag{31}$$

$$x_b = \sqrt{\frac{c_4 - \sqrt{c_4^2 - c_6}}{c_6}} \,, \tag{32}$$

$$x_c = \sqrt{\frac{c_4 + \sqrt{c_4^2 - c_6}}{c_6}} \,, \tag{33}$$

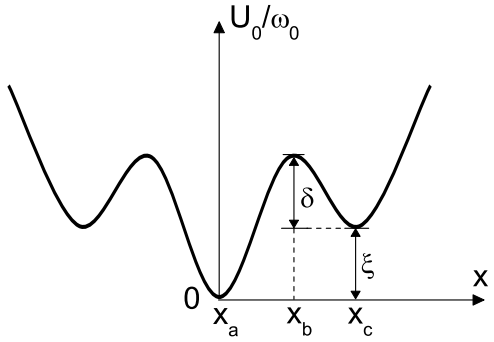

Fig. 5. On-site potential U_0 for the modified Krumhansl-Schrieffer model in the unit of ω_0. The coordinates of potential extrema are denoted by x_a, x_b, and x_c. δ and ξ are two parameters adopted to characterize this potential.

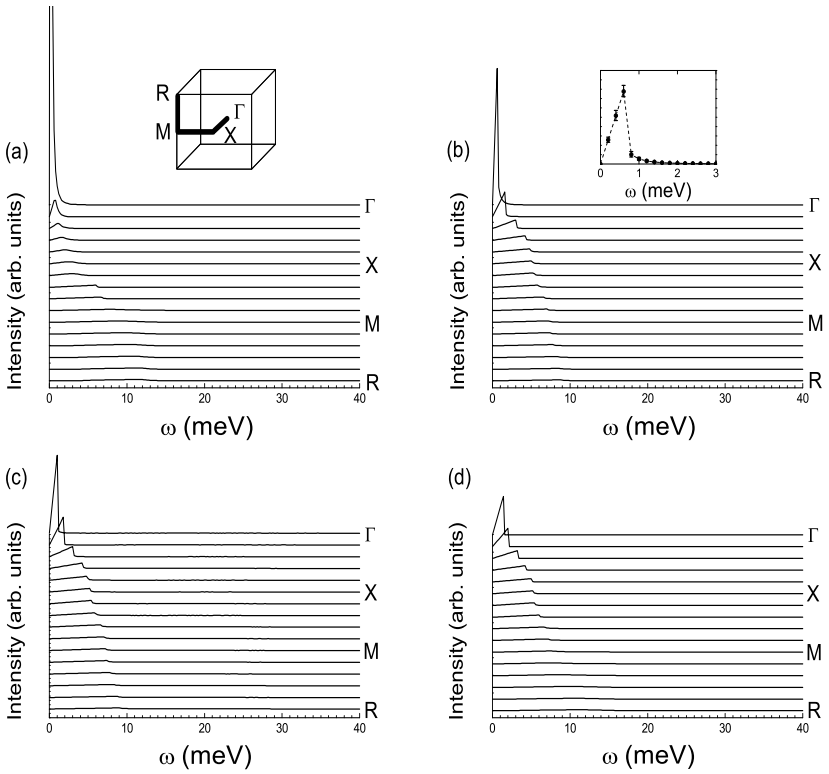

Fig. 6. Phonon spectral function along the line ΓXMR of Brillouin zone in the paraelectric phase at various temperatures: (a) $1.001T_c$, (b) $1.012T_c$, (c) $1.059T_c$, and (d) $1.176T_c$, where T_c=386 K. The inset of panel (a) shows the Brillouin zone with high symmetry lines. The inset of panel (b) represents the spectrum at Γ point when T=1.012 T_c.

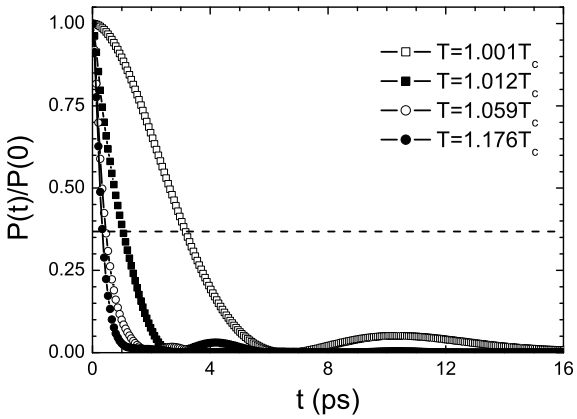

Fig. 7. Normalized speckle scattering probability as a function of time for paraelectric $BaTiO_3$, at various temperatures. Horizontal dashed line denotes $P(t)=P(0)/e$.

In Figs. 6 and 7, we show the optical responses of crystal, where c_4=2.0132x10^{-2} and c6=3.2595×10^{-4} are used. Fig. 6 presents the phonon spectral functions in the paraelectric phase at different temperatures: (a) T=1.001T_c, (b) T=1.012T_c, (c) T=1.059T_c and (d) T=1.176T_c, where T_c=386 K. In each panel, the spectra are arranged with wave vectors along the ΓXMR direction of Brillouin zone [see in the inset of panel (a)], and ω refers to energy. In the inset of panel (b), the spectrum at Γ point for T=1.012T_c is plotted. Since the spectra are symmetric with respect to the origin ω=0, here we only show the positive part of them. In Fig. 6, when the temperature decreases towards T_c, as already well-known for the displacive type phase transition, the energy of phonon peak is gradually softened. In addition, a so-called central peak, corresponding to the low energy excitation of ferroelectric cluster, appears at the Γ point. The collective excitation represented by this sharp resonant peak is nothing but the photo-created ferroelectric cluster. On decreasing temperature, spontaneous polarization is developed locally as a dipole fluctuation in the paraelectric phase. This fluctuation can stabilize the photo-created ferroelectric cluster, leading to a dramatically enhanced peak intensity near T_c.

The appearance of sharp peak at Γ point nearby T_c signifies a long life-time of the photo-created ferroelectric clusters after irradiation. Thus, near T_c, they are more likely to be probed by subsequent laser pulse, resulting in a high intensity of speckle pattern. Keeping this in mind, we move on to the results of scattering probability. In Fig. 7, we show the variation of normalized probability $P(t)/P(0)$ as a function of t (time interval between the pump and probe photons). Temperatures for these curves correspond to those in the panels (a)-(d) of Fig. 6, respectively. In this figure, $P(t)/P(0)$ declines exponentially, showing that the speckle correlation decreases with t increases as a result of the photorelaxation of ferroelectric cluster. When t is long enough, the crystal returns to the equilibrium paraelectric state. In addition, as shown in the figure, the relaxation rate bears a temperature dependence. On approaching T_c, the duration for return is prolonged, indicative of a critical slowing down of the relaxation. This is because with the decrease of temperature, the fluctuation of local polarization is enhanced, and a long range correlation between dipole moments is to be established as well, making the relaxation of photo-created clusters slower and slower.

3.2 Critical slowing down of photorelaxation

In order to quantitatively depict the critical slowing down, we introduce a relaxation time t_r to estimate the time scale of relaxation, which is the time for $P(t)$ to be reduced by a factor of e from $P(0)$. In Fig. 7, $P(t)=P(0)/e$ is plotted by a horizontal dashed line. Correspondingly, t_r is the abscissa of the intersection point of relaxation curve and this dashed line. In Fig. 8, the relaxation time for various local potential U_0 is presented at $T>T_c$. Here we adopt two legible parameters, δ and ξ, to describe the potential wells and barriers for U_0 (see Fig. 5), which are defined by

$$\delta = \frac{U_0(x_b) - U_0(x_c)}{\omega_0}, \tag{34}$$

$$\xi = \frac{U_0(x_c)}{\omega_0}. \tag{35}$$

Provided δ and ξ, c_4 and c_6 can be derived in terms of Eqs. (32)-(35). The values of c_4 and c_6 for the calculation of Fig. 8 are listed in Table 1, where we set ξ=3.061 and change δ from 4.239 to 4.639. The leftmost point on each curve denotes the t_r at just above T_c, which is a temperature determined from the singular point of C_f^V according to Eq. (28).

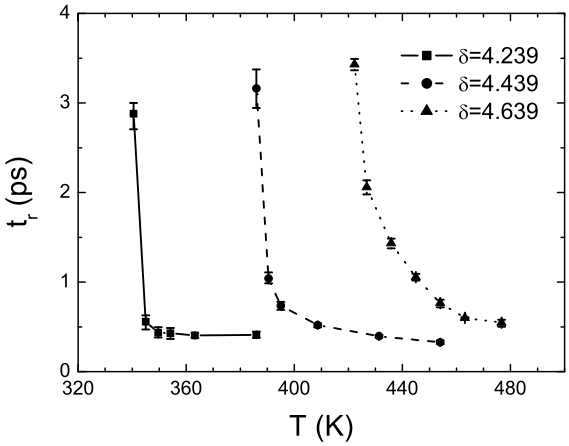

Fig. 8. Temperature dependence of relaxation time t_r for various δ when $T>T_c$, where ξ is fixed at 4.439.

As revealed by the NMR experiment (Zalar et al., 2003), the paraelectric-ferroelectric phase transition of $BaTiO_3$ has both displacive and order-disorder components in its mechanism. Short range dipole fluctuation arises in the paraelectric phase near T_c as a precursor of the order-disorder transition, and condenses into long range ferroelectric ordering below T_c. Thus, in the present study, the relaxation of photo-created cluster is also subject to the dynamics of this dipole fluctuation and yields a temperature dependence. As illustrated by the three curves in Fig. 8, if a ferroelectric cluster is created at a temperature close to T_c, relaxation of this cluster is slow because of a rather strong dipole fluctuation, which holds the cluster in the metastable ferroelectric state from going back to the paraelectric one. Away

from T_c, t_r decreases considerably for the dipole fluctuation is highly suppressed. This behaviour is nothing but the critical slowing down of photorelaxation.

c_4	c_6	δ	ξ	T_c (K)
2.0696×10^{-2}	3.4521×10^{-4}	4.239	3.061	340
2.0132×10^{-2}	3.2593×10^{-4}	4.439	3.061	386
1.9596×10^{-2}	3.0814×10^{-4}	4.639	3.061	422

Table 1. Parameters adopted for calculation of Fig. 8.

In Fig. 8, it can also be seen that with the increase of δ, T_c moves to the high temperature side so as to overcome a higher potential barrier between the ferroelectric and paraelectric phases. Furthermore, the evolution of t_r becomes gentle as well, implying a gradual weakening of dipole fluctuation at high temperature region.

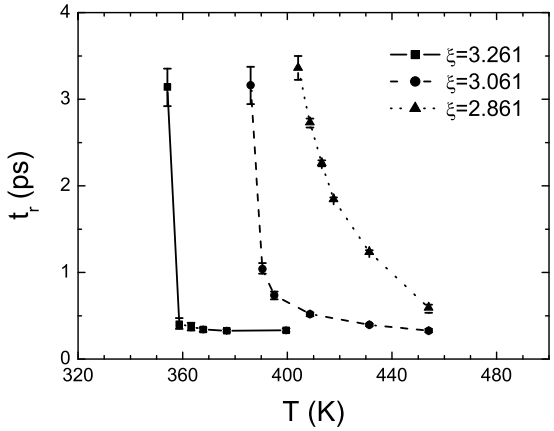

Fig. 9. Temperature dependence of relaxation time t_r for various ξ when $T>T_c$, where δ is fixed at 3.061.

In Fig. 9, we show the temperature dependence of t_r for different ξ when $T>T_c$, where δ is fixed at 4.439. The values of parameters for this calculation are given in Table 2. When ξ changes from 3.261 to 2.861, as shown in Fig. 9, T_c gradually increases. This is because with the decrease of ξ, the ferroelectric state at x_c (refer to Fig. 5) becomes more stable and can survive even larger thermal fluctuation. In a manner analogous to Fig. 6, the evolution of t_r also displays a sharp decline at low temperature, and becomes more and more smooth as temperature increases.

c_4	c_6	δ	ξ	T_c (K)
1.9626×10^{-2}	3.1070×10^{-4}	4.439	3.261	354
2.0132×10^{-2}	3.2593×10^{-4}	4.439	3.061	386
2.0663×10^{-2}	3.4223×10^{-4}	4.439	2.861	404

Table 2. Parameters adopted for calculation of Fig. 9.

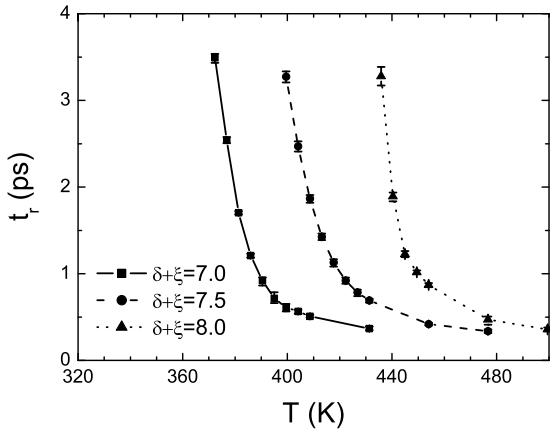

Fig. 10. Temperature dependence of relaxation time t_r for various barrier height $\delta+\xi$ when $T>T_c$, where $\delta/\xi=1.5$ is assumed.

In Fig. 10, we plot the temperature dependence of t_r for different barrier heights, i.e., $\delta+\xi$ varies from 7.0 to 8.0, while the ratio of δ/ξ is fixed at 1.5. Parameters for this calculation are provided in Table 3. As already discussed with Figs. 8 and 9, a larger δ tends to increases T_c, but a higher ξ applies an opposite effect on T_c. Combining these two effects, in Fig. 10, one finds that T_c increases if both δ and ξ are enhanced, indicating that in this case, the change of δ plays a more significant role than that of ξ. Meanwhile, in contrast to Figs. 8 and 9, all the three curves in Fig. 10 present smooth crossovers on decreasing temperature towards T_c, signifying that the dipole fluctuation can be promoted by lowering ξ even the temperature is decreased.

c_4	c_6	δ	ξ	$\delta+\xi$	T_c (K)
2.1557×10^{-2}	3.7309×10^{-4}	4.200	2.800	7.000	372
2.0122×10^{-2}	3.2505×10^{-4}	4.500	3.000	7.500	400
1.8860×10^{-2}	2.8557×10^{-4}	4.800	3.200	8.000	436

Table 3. Parameters adopted for calculation of Fig. 10.

In Namikawa's experiment, the wavelength of soft x-ray laser is 160 Å, hence the photo-created polarization cluster is of nano scale. However, it should be noted that relaxation process of such a nano-sized cluster is actually beyond our present quantum Monte Carlo simulations because of the size limitation of our model. For small-scale dipole fluctuations, the relaxation becomes relatively fast. This is the primary reason why the experimentally measured relaxation time can reach about 30 picoseconds, being several times longer than our calculated results. In spite of the difference, our calculation has well clarified the critical dynamics of $BaTiO_3$ and the origin of speckle variation.

4. Conclusion

We carry out a theoretical investigation to clarify the dynamic property of photo-created ferroelectric cluster observed in the paraelectric $BaTiO_3$ as a real time correlation of speckle

pattern between two soft x-ray laser pulses. The density matrix is calculated by a perturbative expansion up to the fourth order terms, so as to characterize the time dependence of scattering probability. The cluster-associated phonon softening as well as central peak effects are well reproduced in the phonon spectral function via a quantum Monte Carlo simulation. We show that the time dependence of speckle pattern is determined by the relaxation dynamics of photo-created ferroelectric cluster, which is manifested as a central peak in the phonon spectral function. The photorelaxation of ferroelectric cluster is featured by a critical slowing down on decreasing the temperature. Near the T_c, cluster excitation is stablized by the strong dipole fluctuation, correspondingly the relaxation becomes slow. While, at higher temperature, dipole fluctuation is suppressed, ending up with a quicker relaxation of cluster. Our simulation also illustrates that the critical slowing down and dipole fluctuation are subject to the chemical environment of crystal.

5. Acknowledgments

We are indebted to Professor K. Namikawa and Professor H. Zheng for their valuable discussions. This work is supported by the Ministry of Education, Culture, Sports, Science and Technology of Japan, the peta-computing project, and Grant-in-Aid for Scientific Research (S), Contract No. 19001002, 2007.

6. Appendices

6.1 Hybrid Monte Carlo method

The Metropolis algorithm is a widely used sampling rule for the Monte Carlo simulation. It randomly generates a new configuration from the previous one and accept it with the probability min[1,exp(-ΔE)], where ΔE is the energy difference between the initial and final configurations. In the present case of interacting many-body system, however, the Metropolis algorithm works only slowly, because we have to sum up a great number of paths and the phonon coordinate covers a large spatial extent. Nevertheless, we find the so-called hybrid Monte Carlo algorithm (Duane et al., 1987) is very efficient. By introducing an extra degree of freedom, it adequately combines the heat bath scheme with the Metropolis algorithm so as to achieve a rapid and ergodic evolution through the configuration space.

In order to incorporate this hybrid Monte Carlo algorithm to our path-integral theory, we first discretize the imaginary time τ, dividing β into L segments with interval Δ. Then, from Eqs. (24) and (26) we write the partition function (≡Z) as,

$$Z = e^{-\beta \Phi_f} = \int Dx \exp\left\{-\int_0^\beta d\tau \Omega_f[x(\tau)]\right\}$$

$$= \int Dx \exp\left\{-\Delta \sum_{i=1}^{L} \Omega_f(x_i)\right\}. \tag{36}$$

Then we introduce a "pseudo time" t, and velocity field $\dot{x}$, which is the derivative of x with respect to this pseudo time. Then, we define a new pseudo crystal with its partition function (≡Z_P) given by

$$Z_P = Z \int D\dot{x} \exp\left(-\sum_{i,l} \frac{\dot{x}_{i,l}^2}{2}\right)$$

$$= \int DxD\dot{x}e^{-H_P(x,\dot{x},t)} , \tag{37}$$

where i and l refer to imaginary time τ and real lattice site, respectively, and

$$H_P(x,\dot{x},t) = \sum_{i,l}\left[\frac{\dot{x}_{i,l}^2}{2} + \frac{1}{2\omega_0\Delta}(x_{i,l} - x_{i-1,l})^2 + \frac{\Delta}{2}\omega_0 x_{i,l}^2 - \frac{\Delta}{2}\omega_0 c_4 x_{i,l}^4 + \frac{\Delta}{6}\omega_0 c_6 x_{i,l}^6\right]$$

$$-\frac{\Delta}{2}\omega_0 d_2 \sum_{i,<l,l'>} x_{i,l}x_{i,l'} . \tag{38}$$

Because the Gaussian noise in Eq. (37) can be integrated out of the partition function Z_P, the introduction of the auxiliary degree of freedom actually gives no effect on the thermal average involving x, and the new configurations for Monte Carlo sampling thus can be determined by the Hamilton's principle

$$\delta\int_{t_1}^{t_2} L_P(x,\dot{x},t)dt = 0 , \tag{39}$$

where t_1 and t_2 are the initial and final pseudo times, respectively, and L_P is the Lagrangian of the pseudo crystal defined as

$$L_P(x,\dot{x},t) = \sum_{i,l} x_{i,l}^2 - H_P(x,\dot{x},t) . \tag{40}$$

Expanding Eq. (39) with respect to δx and $\delta\dot{x}$, we obtain the ordinary Hamilton's equation

$$\ddot{x}_{i,l} = -\frac{\partial H_P(x,\dot{x},t)}{\partial x_{i,l}} . \tag{41}$$

To generate the new configurations, the following scheme of molecular dynamics is cycled. For a given set of x, we first update $\dot{x}$ field using a heat bath, i.e., set each $\dot{x}_{i,l}$ to be a random number of Maxwell-Boltzmann distribution. Next we propagate x and $\dot{x}$ forward along pseudo time t according to the Hamilton's equation (41). To this end, we divide the time interval into N_t molecular-dynamics steps, which is 20 ~ 40 in this work. Compute $\dot{x}$ at $\frac{1}{2}\delta t$, $\frac{1}{2}\delta t$, $\frac{5}{2}\delta t$, …, $(N_t - \frac{1}{2})\delta t$, $N_t\delta t$ [$\delta t \equiv (t_2 - t_1)/N_t$] and x at δt, $2\delta t$, $3\delta t$, …, $N_t\delta t$ by the "leap-frog" algorithm (Allen & Tildesley, 1989). Then this evolved configuration is accepted according to the Metropolis algorithm.

6.2 Iterative fitting method

With the Green's function calculated by the QMC simulation, the phonon spectral function $A(\omega)$ can be numerically attained by the analytic continuation of Eq. (30). Before we proceed to calculate the phonon spectral function, in this section, we first address how to derive the spectral function of electron. We shall see, the electron-oriented iterative fitting algorithm developed here is the cornstone for a more general approach towards solving the problem of spectrum reconstruction, like that related with phonon.

In the case of electron, the spectral function $A(\omega)$ is connected to the electronic Green's function $G(\tau)$ by an equation similar to Eq. (30),

$$G(\tau) = -\int_{-\infty}^{\infty} \frac{e^{-\tau\omega}}{1+e^{-\beta\omega}} A(\omega) d\omega \,. \tag{42}$$

In terms of Eq. (42), the numerical calculation starts from the following equation,

$$G_i = \sum_j K_{ij} A_j \Delta\omega \,. \tag{43}$$

where i and j denote the discretized imaginary time τ and frequency ω, respectively, and

$$K_{ij} = -\frac{e^{-\tau_i \omega_j}}{1+e^{-\beta\omega_j}} \tag{44}$$

is the integral kernel. In order to perform this analytic continuation efficiently, we have developed an iterative fitting method (Ji et al., 2004), which can reproduce the normalized and positive-definite spectra self-consistently. Our algorithm is based on the sum-rule of electronic spectrum (Mahan, 1990)

$$\sum_j A_j \Delta\omega = 1 \,, \tag{45}$$

which suggests that the spectral function can be rewritten in an iterative form as

$$A_j^{(N)} = \frac{n_j^{(N)}}{N\Delta\omega} \,, \tag{46}$$

where $n_j^{(N)}$ is the bin counter for the j-th spectral segment $A_j^{(N)}$ and records the times that the j-th bin being used during the previous N iterative steps. The sum rule of Eq. (45) is thus fulfilled by

$$N = \sum_j n_j^{(N)} \,. \tag{47}$$

The positivity of $A_j^{(N)}$ is also guaranteed because $n_j^{(N)}$ is nonnegative.
To reproduce the spectral function, we start from a flat spectrum, and then repeat the following scheme:
(1) First we calculate the Green's function $G_i^{(N)}$ by the current spectral function $A_j^{(N)}$ as,

$$G_i^{(N)} = \sum_j K_{ij} A_j^{(N)} \Delta\omega \,. \tag{48}$$

(2) Then measure the distance [$\equiv\chi^{(N)}$] between $G_i^{(N)}$ and the true G_i (QMC results) as

$$\left[\chi^{(N)}\right]^2 = \sum_i \left[G_i^{(N)} - G_i\right]^2 \,, \tag{49}$$

which finally should be minimized by the present iteration.
(3) Make a trial spectral function $A_j^{(N+1)}$ of the next step $N+1$, whose $n_j^{(N+1)}$ is different from $n_j^{(N)}$ by only one, and only in a randomly selected bin j_0, as

$$n_j^{(N+1)} = n_j^{(N)} + \delta_{jj_0} \,. \tag{50}$$

By this change, we have new $A_j^{(N+1)}$, $G_i^{(N+1)}$ and $\left[\chi^{(N+1)}\right]^2$ for this trial step.
(4) Calculate the difference S as

$$S = \left[\chi^{(N)}\right]^2 - \left[\chi^{(N+1)}\right]^2 + \sum_i \left[G_i^{(N+1)} - G_i^{(N)}\right]^2 . \tag{51}$$

(5) If S>0, we accept the change Eq. (50), and start a new cycle from (1). Otherwise, reject this change Eq. (50) and return to (3).
Here let us explain the meaning of S of Eq. (51). In Eq. (49), $\chi^{(N)}$ gives the distance from the true **G** to the trial $\mathbf{G}^{(N)}$, in a hyperspace spanned by various **G**'s, $\mathbf{G}^{(N)}$'s and $\mathbf{G}^{(N+1)}$'s, as schematically shown in Fig. 11. The equi-distant sphere is also symbolically denoted by S_1 in this figure. If $\chi^{(N)}>\chi^{(N+1)}$, or $\mathbf{G}^{(N+1)}$ is in this sphere S_1, we, of course, have to accept this change Eq. (50) unconditionally, since the distance becomes shorter than before.
However, $\chi^{(N)}$ may not be a simple function of this change (≡**Δ**),

$$\mathbf{\Delta} \equiv \mathbf{G}^{(N+1)} - \mathbf{G}^{(N)} , \tag{52}$$

but will be a nonlinear and complicated function. In some cases, $\chi^{(N)}$ will be in a local minimum with respect to the change **Δ**, and this change cannot make the distance shorter. For this reason, in Eq. (51), we introduce a "relaxation effect" through the third term, which avoids the search for $\chi_{\min}^{(N)}$ being trapped in such a local minimum. Since the projection of **Δ** on the vector $\mathbf{G}^{(N)}$-**G** is just $-S/2\chi^{(N)}$, we find that the acceptable region for the trial $\mathbf{G}^{(N+1)}$ consists of two sections, i.e., i and ii (see in Fig. 11), both of which correspond to S>0. In section i, $\mathbf{G}^{(N+1)}$ is unconditionally accepted, since $\chi^{(N+1)}$ truly decreases. While in section ii, the acceptance is conditional, since it does not give a smaller $\chi^{(N+1)}$ but only make $\mathbf{G}^{(N+1)}$ moves toward **G** along the **G**-$\mathbf{G}^{(N)}$ line. By taking this conditional acceptance, the minimization is relaxed, and correspondingly an uphill search for a more global minimum can be continued.
With the algorithm described above, the spectral function can be readily recovered from the Green's function. A few hundred iterations are sufficient to construct the convergent spectra, but with very rough contours. For a naturally refined line shape, much more iterations are necessary before no appreciable change can be observed any more.

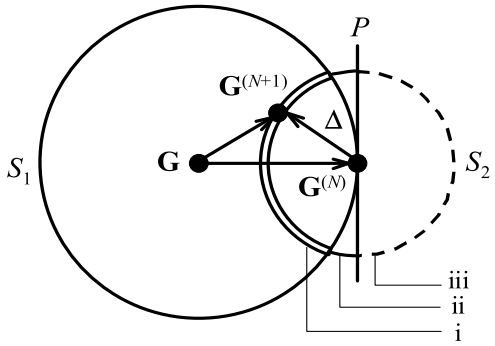

Fig. 11. Schematic interpretation for the recipe of analytic continuation. The hypersphere S_1 is centered at **G** with radius $\chi^{(N)}$, and S_2 is centered at $\mathbf{G}^{(N)}$ with radius $|\mathbf{\Delta}|$. The hyperplane P is perpendicular to $\mathbf{G}^{(N)}$-**G** and bisects S_2. The surface of S_2 is thus composed of three sections: i (unconditional acceptance), ii (conditional acceptance) and iii (rejection).

6.3 Renormalization iterative fitting method

The iterative fitting method relies its convergence on the sum-rule of electronic spectrum, which conserves the total spectral weight through the iteration process. In a same manner, the Green's function and spectral function can be introduced to describe a bosonic system. It can be shown that in the case of boson, Eq. (42) should be reformulated as

$$G(\tau) = -\int_{-\infty}^{\infty} \frac{e^{-\tau\omega}}{1-e^{-\beta\omega}} A(\omega) d\omega \,, \tag{53}$$

and the sum rule also holds for the bosonic spectrum $A(\omega)$. Hence we can apply the iterative fitting method to calculate it.

However, for the phonon spectrum, there is not a rule that conserves the total spectral sum like that of electron. This is because the phonon Green's function is defined in the coordinate representation rather the particle number representation [see Eqs. (17) and (20)]. Such a definition leads to general properties of phonon spectrum as manifested by

$$\omega A(\omega) \geq 0 \,, \tag{54}$$

$$A(-\omega) = -A(\omega) \,. \tag{55}$$

Obviously, the phonon spectrum is anti-symmetric and the total sum of spectral weight should be zero,

$$\int_{-\infty}^{\infty} A(\omega)\, d\omega = 0 \,. \tag{56}$$

Therefore, the standard iterative fitting method does not work for phonon.

In order to get the phonon spectral function $A(\omega)$, we need to confine our calculation in the region $0<\omega<\infty$, and introduce a renormalized spectral function $\tilde{A}(\omega)$ as

$$\tilde{A}(\omega) \equiv -\frac{1}{G(\beta)} \coth\left(\frac{1}{2}\beta\omega\right) A(\omega) \,. \tag{57}$$

Because of the anti-symmetry of $A(\omega)$, the integral in Eq. (53) can be rewritten as

$$G(\tau) = \int_0^{\infty} \frac{1}{\cosh\left(\frac{1}{2}\beta\omega\right)} \cosh\left[\left(\frac{1}{2}\beta - \tau\right)\omega\right] G(\beta)\tilde{A}(\omega) d\omega \,. \tag{58}$$

It is easy to see the renormalized spectral function is positive if $\omega>0$, and satisfies a sum rule,

$$\int_0^{\infty} \tilde{A}(\omega)\, d\omega = 1 \,, \tag{59}$$

which allow us to solve the integral equation of Eq. (58) by the iterative fitting approach in the region $0<\omega<\infty$. Once $\tilde{A}(\omega)$ is reproduced, the phonon spectral function $A(\omega)$ can be obtained from Eq. (57).

7. References

Allen, M.P. & Tildesley, D.J. (1989). *(1987). Computer simulation of liquids*, Clarendon, ISBN 0198556454, Oxford

Aubry, S. (1975). A unified approach to the interpretation of displacive and order–disorder systems. I. Thermodynamical aspect, *Journal of Chemical Physics*, 62, 3217-3229, ISSN 0021-9606

Bonča, J. & Gubernatis, J.E. (1996). Real-time dynamics from imaginary-time quantum Monte Carlo simulations: Tests on oscillator chains, *Physical Review B*, 53, 6504-6513, ISSN 1098-0121

Doniach, S. & Sondheimer, E.H. (1998). *Green's Functions for Solid State Physicists*, Imperial College Press, ISBN 1860940781, London

Duane, S.; Kennedy, A.D.; Pendleton, B.J. & Roweth, D. (1987). Hybrid Monte Carlo, *Physics Letters B*, 195, 216-222, ISSN 0370-2693

Goodman, J. W. (2007). *Speckle Phenomena in Optics: Theory and Applications*, Roberts & Company, ISBN 0974707791, Greenwood Village

Gubernatis, J.E.; Jarrell, M.; Silver, R.N. & Sivia, D.S. (1991). Quantum Monte Carlo simulations and maximum entropy: dynamics from imaginary-time data, *Physical Review B*, 44, 6011-6029, ISSN 1098-0121

Hamazaki, S.-I.; Shimizu, F.; Kojima, S. & Takashige, M. (1995). AFM observation of 90° domains of $BaTiO_3$ butterfly crystals, *Journal of the Physical Society of Japan*, 64, 3660-3663, ISSN 0031-9015

Harada, J.; Axe, J.D. & Shirane, G. (1971). Neutron-scattering study of soft modes in cubic $BaTiO_3$, *Physical Review B*, 4, 155-162, ISSN 1098-0121

Ji, K.; Zheng, H. & Nasu, K. (2004). Path-integral theory for evolution of momentum-specified photoemission spectra from broad Gaussian to two-headed Lorentzian due to electron-phonon coupling, *Physical Review B*, 70, 085110(1-9), ISSN 1098-0121

Ji, K.; Namikawa, K; Zheng, H. & Nasu, K. (2009). Quantum Monte Carlo study on speckle variation due to photorelaxation of ferroelectric clusters in paraelectric barium titanate, *Physical Review B*, 79, 144304(1-8), ISSN 1098-0121

Khare, A. & Saxena, A. (2008). Domain wall and periodic solutions of a coupled φ^6 model, *Journal of Mathematical Physics*, 49, 063301(1-18), ISSN 0022-2488

Kishimoto, M.; Namikawa, K.; Sukegawa, K.; Yamatani, H; Hasegawa, N. & Tanaka M. (2010). Intensity correlation measurement system by picosecond single shot soft x-ray laser, *Review of Scientific Instruments*, 81, 013905(1-5), ISSN 0034-6748

Krausz, F. & Ivanov, M. (2009). Attosecond physics, *Review of Modern Physics*, 82, 162-234, ISSN 0034-6861

Krumhansl, J.A. & Schrieffer, J.R. (1975). Dynamics and statistical mechanics of a one-dimensional model Hamiltonian for structural phase transitions, *Physical Review B*, 11, 3535-3545, ISSN 1098-0121

Mahan, G.D. (1990). *Many-Particle Physics*, 2nd ed., Plenum, ISBN 1441933395, New York

May, M. (1977). Information inferred from the observation of speckles. *Journal of Physics E: Scientific Instruments,* 10, 849-864, ISSN 0022-3735

Migoni, R.; Bauer, D. & Bilz, H. (1976). Origin of Raman scattering and ferroelectricity in oxidic perovskites, *Physical Review Letter*, 37, 1155-1158, ISSN 0031-9007

Morris, J.R. & Gooding, R.J. (1990). Exactly solvable heterophase fluctuations at a vibrational-entropy-driven first-order phase transition, *Physical Review Letter*, 65, 1769-1772, ISSN 0031-9007

Mulvihill, W.L.; Uchino, K.; Li, Z. & Cao, W. (1996). In-situ observation of the domain configurations during the phase transitions in barium titanate, *Philosophical Magazine B*, 74, 25-36, ISSN 1364-2812

Namikawa, K.; Kishimoto, M.; Nasu, K.; Matsushita, E.; Tai, R.Z.; Sukegawa, K.; Yamatani, H.; Hasegawa, H.; Nishikino, M.; Tanaka, M. & Nagashima, K. (2009). Direct Observation of the Critical Relaxation of Polarization Clusters in $BaTiO_3$ Using a Pulsed X-Ray Laser Technique, *Physical Review Letter,* 103, 197401(1-4), ISSN 0031-9007

Nasu, K. (1994). Resonance enhancement of inelastic x-ray scatterings induced by strong visible lights, *Journal of the Physical Society of Japan*, 63, 2416-2427, ISSN 0031-9015

Pang, G.K.H. & Baba-Kishi, K.Z. (1998). Characterization of butterfly single crystals of $BaTiO_3$ by atomic force, optical and scanning electron microscopy techniques, *Journal of Physics D: Applied Physics*, 31, 2846-2853, ISSN 0022-3727

Polla, D.L. & Francis, L.F. (1998). Processing and characterization of piezoelectric materials and integration into microelectromechincal systems, *Annual Review of Materials Science*, 28, 563-597, ISSN 0084-6600

Savkin, V.V.; Rubtsov, A.N. & Janssen, T. (2002). Quantum discrete φ^4 model at finite temperatures, *Physical Review B*, 65, 214103(1-12), ISSN 1098-0121

Schneider, T. & Stoll, E. (1978). Molecular-dynamics study of a three-dimensional one-component model for distortive phase transitions, *Physical Review B*, 17, 1302-1322, ISSN 1098-0121

Skilling, J. & Bryan, R.K. (1984). Maximum entropy image reconstruction: general algorithm, *Monthly notices of the royal astronomical society*, 211, 111-124, ISSN 0035-8711

Tai, R.Z.; Namikawa, K.; Kishimoto, M.; Tanaka, M.; Sukegawa, K.; Hasegawa, N.; Kawachi, T.; Kado, M.; Lu, P.; Nagashima, K.; Daido, H.; Maruyama, H.; Sawada, A.; Ando, M. & Kato, Y. (2002). Picosecond snapshot of the speckles from ferroelectric $BaTiO_3$ by means of x-ray lasers, *Physical Review Letter*, 89, 257602(1-4), ISSN 0031-9007

Tai, R.Z.; Namikawa, K.; Sawada, A.; Kishimoto, M.; Tanaka, M.; Lu, P.; Nagashima, K.; Maruyama, H. & Ando, M. (2004). Picosecond view of microscopic-scale polarization clusters in paraelectric $BaTiO_3$, *Physical Review Letter*, 93, 087601(1-4), ISSN 0031-9007

Takagi, M. & Ishidate, T. (2000). Anomalous birefringence of cubic $BaTiO_3$, *Solid State Communications*, 113, 423-426, ISSN 0038-1098

Völkel, G. & Müller, K.A. (2007). Order-disorder phenomena in the low-temperature phase of $BaTiO_3$, *Physical Review B*, 76, 094105(1-8), ISSN 1098-0121

Yamada, Y.; Shirane, G. & Linz, A. (1969). Study of critical fluctuations in $BaTiO_3$ by neutron scattering, *Physical Review*, 177, 848-857, ISSN 0031-899X

Yamazaki, M.; Tomita, N. & Nasu, K. (2003). Intermediately correlated many-electron systems studied by quantum Monte Carlo method, *Journal of the Physical Society of Japan*, 72, 611-617, ISSN 0031-9015

Yan, R.; Guo, Z.; Tai, R.; Xu, H.; Zhao, X.; Lin, D.; Li, X. & Luo, H. (2008). Observation of long range correlation dynamics in $BaTiO_3$ near T_C by photon correlation spectroscopy, *Applied Physics Letters*, 93, 192908(1-3), ISSN 0031-9007

Yin, Q.R.; Zeng, H.R.; Yu, H.F. & Li, G.R. (2006). Near-field acoustic and piezoresponse microscopy of domain structures in ferroelectric material, *Journal of Materials Science*, 41, 259-270, ISSN 0022-2461

Zalar, B.; Laguta, V.V. & Blinc, R. (2003). NMR evidence for the coexistence of order-disorder and displacive components in barium titanate, *Physical Review Letter*, 90, 037601(1-4), ISSN 0031-9007

Zhong, W.; King-Smith, R.D. & Vanderbilt, D. (1994). Giant LO-TO splittings in perovskite ferroelectrics, *Physical Review Letter*, 72, 3618-3662, ISSN 0031-9007

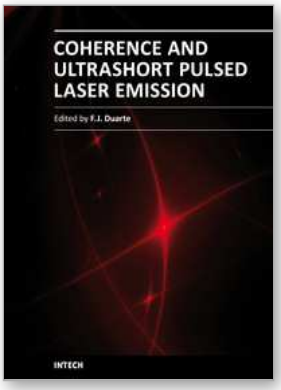

Coherence and Ultrashort Pulse Laser Emission

Edited by Dr. F. J. Duarte

ISBN 978-953-307-242-5
Hard cover, 688 pages
Publisher InTech
Published online 30, November, 2010
Published in print edition November, 2010

In this volume, recent contributions on coherence provide a useful perspective on the diversity of various coherent sources of emission and coherent related phenomena of current interest. These papers provide a preamble for a larger collection of contributions on ultrashort pulse laser generation and ultrashort pulse laser phenomena. Papers on ultrashort pulse phenomena include works on few cycle pulses, high-power generation, propagation in various media, to various applications of current interest. Undoubtedly, Coherence and Ultrashort Pulse Emission offers a rich and practical perspective on this rapidly evolving field.

How to reference

In order to correctly reference this scholarly work, feel free to copy and paste the following:

Kai Ji and Keiichiro Nasu (2010). Probing Ultrafast Dynamics of Polarization Clusters in $BaTiO_3$ by Pulsed Soft X-Ray Laser Speckle Technique, Coherence and Ultrashort Pulse Laser Emission, Dr. F. J. Duarte (Ed.), ISBN: 978-953-307-242-5, InTech, Available from: http://www.intechopen.com/books/coherence-and-ultrashort-pulse-laser-emission/probing-ultrafast-dynamics-of-polarization-clusters-in-batio3-by-pulsed-soft-x-ray-laser-speckle-tec

INTECH
open science | open minds

InTech Europe
University Campus STeP Ri
Slavka Krautzeka 83/A
51000 Rijeka, Croatia
Phone: +385 (51) 770 447
Fax: +385 (51) 686 166
www.intechopen.com

InTech China
Unit 405, Office Block, Hotel Equatorial Shanghai
No.65, Yan An Road (West), Shanghai, 200040, China
中国上海市延安西路65号上海国际贵都大饭店办公楼405单元
Phone: +86-21-62489820
Fax: +86-21-62489821